Short-range repulsive force model for near-contact interactions of bubbles

Lingxin Zhang, Kai Peng ⬤, Xueming Shao ⬤, and Jian Deng ⬤*

State Key Laboratory of Fluid Power and Mechatronic Systems, Department of Mechanics, Zhejiang University, Hangzhou 310027, China

We introduce a short-range repulsive force model to tackle near-contact interactions when the collision occurs between bubbles. In contrast to the previous numerical method adopting the adaptive mesh refinement technique, such a mesoscale model can be applied to a relatively coarse mesh, which can prevent the nonphysical coalescence between bubbles without excessive mesh refinement. We assume that the repulsive force is inversely proportional to the third power of distance, as a reasonable approximation to the short-range phase interactions. The model is validated against two different experiments. In both experiments, two identical bubbles rising side by side were considered. First, the experiment performed in a water-glycerol mixture helps determine the model parameter K. Second, three typical combinations of bubble size and initial separation distance are simulated, presenting different types of interactions, i.e., coalescence, bouncing coalescence, and bouncing separation, agreeing well with the second experiment, which was performed in pure water. Owing to its simplicity, this model can be easily implemented into existing codes, and it can be extended to the case with multiple bubbles or droplets.

I. INTRODUCTION

The dynamics of coalescence and/or repulsion between bubbles has intrigued scientists and engineers for many years owing to its ubiquitousness in natural processes and engineering applications, such as air bubble dispersion in oceans, enhanced heat and mass transfer by injecting bubbles in chemical and energy industries, and many others [1]. Its underlying physical mechanisms have been elucidated by experiments [1–5] in the past decades. The rapidly increasing capability of high-performance computing enables researchers to understand the richer physics using high-fidelity direct numerical simulations (DNS). For gas-liquid flows including bubbles, a variety of DNS methods have been proposed to track the interfaces, such as front-tracking (FT) [6], volume-of-fluid (VOF) [7,8], phase-field (PF) [9,10], and level-set (LS) methods [11]. The FT method utilizes two separate meshes for the two different phases, making it difficult to consider the coalescence between bubbles unless involving an extra subgrid model. In principle, the other aforementioned methods can capture the coalescence of bubbles. However, they depend strongly on the spatial mesh resolution. It is easy to understand that, as two bubbles approach each other, nonphysical (or numerical) coalescence occurs when their distance is less than one cell size [12]. Physically, as two bubbles move toward each other, when they are very close, a thin liquid film is formed in the gap, which requires a certain drainage time before the occurrence of coalescence. This problem involves an enormously large span of length scales [13]: from the largest scale of bulk flow structure to the smallest scale, the thickness of the liquid film. Usually,

the liquid film can be as thin as a few nanometers, several orders of magnitude smaller than the bubble size [14]. It is challenging to separate these length scales with numerical simulations. For example, the standard front-capturing methods (VOF, PF, and LS) require adaptive local mesh refinement to represent such a thin liquid film and avoid undesirable nonphysical coalescence of bubbles [15,16]. The influence of mesh refinement for a simple two-bubble system has been tested [12], indicating that the cell number could reach up to to 1 billion even in two-dimensional simulations. Apparently, it is unaffordable to simulate the near-contact bubble-bubble interactions in such a way for real applications, when many three-dimensional (3D) bubbles are considered.

In a special scenario, in bubble swarms, since the coalescence or breakup of bubbles plays an insignificant role in their statistic characteristics, numerical algorithms can be proposed to compulsorily avoid the coalescence of bubbles [17]. First, the FT method employs Lagrangian control points to track the interfaces explicitly; therefore, it can naturally avoid the coalescence of bubbles. In extreme cases, when the different Lagrangian control points representing different bubbles coexist in the same mesh cell, they will not extrude each other further due to the fact that they share the same velocities of background fluid. For the front-capturing methods, multiple markers were introduced to distinguish between the different bubbles, then each bubble can be tracked by its own volume fraction field (based on VOF) [18] or signed distance function (based on LS) [14]. Indeed, for this special scenario, as the collisions between bubbles are relatively rare at the low void fraction, and more importantly, people are concerned majorly with the statistic characteristics, instead of the details of bubble-bubble interactions, these numerical treatments have been proved to provide reliable results consistent with the experimental measures [17].

---

*Corresponding author: zjudengjian@zju.edu.cn

However, in some instances, when the interactions between bubbles/droplets or their contact with a substrate are important, the drainage process of the thin film should be resolved. From a microscopic point of view, it is related to the combined action of nanoscale attractive and/or repulsive forces, such as van der Waals and electrostatic forces, steric interactions, and hydration repulsion and depletion attraction [19]. Practically, it can be modeled by introducing a lubrication equation, which has been applied in cases in which the bulk flow is also in microscales [20,21]. Although a considerable amount of theoretical and experimental works have been devoted to describing this complicated process of near interactions within intervening liquid films [22], from a numerical standpoint, the direct introduction of near-interaction forces at a molecular level requires resolving the spatial scales from nanometers to millimeters, which is far beyond the capability of current computing power. It can only be achieved by introducing simplified models. For example, a model accommodating the coalescence and breakup of droplets was implemented in the multiple-marker coupled LS/VOF (CLSVOF) method for head-on collision of two identical droplets [23]. The implemented coalescence model was based on a computationally efficient film drainage model, which predicts if and when two colliding droplets will coalesce. When the contact time between two colliding droplets exceeds the predicted film drainage time, the marker functions of two separate droplets are merged to accomplish the coalescence numerically. Similarly, breakup of a droplet is accommodated by splitting the marker function of the droplet into two [23]. However, this model is not easy to extend to the case with multiple bubbles or droplets.

In this paper, we propose a repulsive force model to describe the near-contact interactions based on a VOF framework, which can control the coalescence of bubbles. The extra forcing added to the momentum equations takes effect only within several mesh cells in the gap of two approaching bubbles, which are easy to identify and track by looping all the bubble-liquid interfaces. To validate this model, a series of 3D simulations are performed considering two rising bubbles side by side, through which an optimal empirical parameter for this model is determined.

The remainder of this paper is organized as follows. The numerical methods with the repulsive near-contact interaction force model and numerical methodology are presented in Sec. II, followed by its validation by using the previous experimental data in Sec. III. Finally, we draw our conclusions in Sec. IV.

II. NUMERICAL METHOD

A. Governing equations

We consider a system consisting of two immiscible, incompressible fluids occupying the space of a computational domain. The state of such a two-phase system is described by a single velocity field $\mathbf{u}(\mathbf{x}, t)$, a pressure field $p(\mathbf{x}, t)$, and dynamically evolved sharp phase interfaces. The differential forms of the continuity and momentum equations are shown in Eqs. (1) and (2), respectively, where ρ and μ are, respectively, the mixture density and dynamic viscosity, taking constant

values in the single-fluid occupied mesh cells, and transiting from that of one fluid to the other at the phase interface. The subscripts f and b represent, respectively, the liquid fluid and gas bubble phases:

$$\nabla \cdot \mathbf{u} = 0, \tag{1}$$

$$\frac{\partial \rho \mathbf{u}}{\partial t} + \nabla \cdot \rho \mathbf{u}\mathbf{u} = -\nabla p - \rho \mathbf{g} + \nabla \cdot \boldsymbol{\tau} + \mathbf{F}_\sigma + \mathbf{F}_{\text{rep}}. \tag{2}$$

The viscous stress tensor $\boldsymbol{\tau}$ is defined by Eq. (3) according to the Newtonian formulation, where $\mathbf{S}$ is the rate-of-strain tensor. Here, $\mathbf{F}_\sigma$ is included to the right side of the momentum equation to represent the surface tension of the liquid-gas interface, which takes the most popular continuum surface force model [24], as shown in Eq. (4), where σ is the surface tension coefficient, δ_s is the Dirac function, and k is the curvature of the interface. Also, $\mathbf{F}_{\text{rep}}$ is an additional repulsive forcing term representing the effects of the near-contact forces operating at the phase interface, of which the details will be elucidated in Sec. II C:

$$\boldsymbol{\tau} = 2\mu \mathbf{S}, \quad S = \frac{1}{2}(\nabla \mathbf{u} + \nabla \mathbf{u}^T), \tag{3}$$

$$\mathbf{F}_\sigma = \sigma k \delta_s \mathbf{n}. \tag{4}$$

B. VOF method

For the VOF method, the volume of one fluid, e.g., the gas phase, is represented by a volume fraction α, governed by the transportation equation, Eq. (5). Thereby, the mixture density and viscosity can be calculated according to Eq. (6):

$$\frac{\partial \alpha}{\partial t} + \mathbf{u} \cdot \nabla \alpha = 0, \tag{5}$$

$$\rho = \alpha \rho_b + (1 - \alpha)\rho_f,$$
$$\mu = \alpha \mu_b + (1 - \alpha)\mu_f. \tag{6}$$

It is a challenge to distinguish two different phases or rebuild a sharp interface in one mesh cell, which is the key issue for VOF methodology. In the past decades, a large variety of VOF schemes have been developed. Most of them can be divided into two categories: the geometric methods, involving an explicit reconstruction of the interface from the volume fraction field [25,26], and the algebraic methods that make no such attempt. Algebraic VOF schemes are typically much simpler, more efficient to implement, and not limited to structured meshes. However, their accuracy is compromised compared with geometric VOF schemes [27].

In this paper, a recently developed geometric algorithm called isoAdvector is implemented to reconstruct and advect the two-phase interfaces [8]. This algorithm consists of two parts: First, an isosurface concept is introduced for modeling the interface inside cells in a geometric surface reconstruction step. Second, for the reconstructed surface, the motion of the face-interface intersection line for a general polygonal face is modeled to obtain the time evolution within a time step of the submerged face area. The total VOF transported across the face can be estimated accurately by integrating this submerged area over the time step. In terms of volume conservation, boundedness, surface sharpness, and efficiency, this algorithm

is satisfactory for the simulations of bubbly flows, where the surface tension plays a nonnegligible role.

The spatial discretizations for the governing equations Eqs. (2) and (5) are second-order upwind for the convection terms and central differences for the Laplacian terms, respectively. The temporal term is discretized by an implicit Crank-Nicolson scheme. The multigrid strategy is involved to accelerate the convergence. The pressure-velocity coupling is obtained by combining the PISO (Pressure Implicit with Splitting of Operators) and SIMPLE (Semi Implicit Method for Pressure Linked Equations) algorithms. The volume fraction transportation equation is solved, with the phase interfaces updated by the isoAdvector algorithm [8].

C. Repulsive force model

Theoretically, across the interface between a bubble and its ambient, the pressure gradient is balanced by the surface tension force, which is given by the classic Young-Laplace equation:

$$\Delta p = \sigma (\nabla \cdot \mathbf{n}), \qquad (7)$$

where Δp is the pressure difference across the fluid interface, σ is the surface tension coefficient, $\nabla \cdot \mathbf{n}$ is the local curvature of phase interface, and $\mathbf{n}$ is the unit vector normal to the interface.

To represent all the repulsive near-contact forces (i.e., van der Waals, electrostatic, steric, and hydration repulsion) acting on much smaller scales than the mesh resolution, the stress-jump condition across a interface can be augmented with a repulsive term to extend the equilibrium for the Young-Laplace equation as follows:

$$\Delta p \mathbf{I} \cdot \mathbf{n} = \sigma (\nabla \cdot \mathbf{n})\mathbf{n} + \mathbf{F}_{\text{rep}}, \qquad (8)$$

where $\mathbf{I}$ is the identity tensor. We now consider an elementary fluid domain Ω, with two bubbles moving toward each other to a very close distance, as shown schematically in Fig. 1. Here, a mesh cell is marked as an interface cell if its volume fraction α is between 0.01 and 0.99. In Fig. 1, we note that the marker points at the interfaces are selected at the cell centers for simplicity, while for generality, these points can be the Lagragian points moving with the interfaces, in which case a redistribution of the repulsive forces from the Lagragian points to the Eulerian cells would be required. In the following content, we use *points* instead of cells.

The additional repulsive term $\mathbf{F}_{\text{rep}}$ is the resultant force acting on the negative direction of the unit normal vector $\mathbf{n}$ of the interfaces between the two phases, which takes effects when the interfaces representing different bubbles move toward each other to a certain close distance. It can be expressed as

$$\mathbf{F}_{\text{rep},i} = -\sum_{j=1'}^{N}(\mathbf{f}_{ij} \cdot \mathbf{n})\mathbf{n} = -\sum_{j=1'}^{N}\frac{K}{h_{ij}^3}\mathbf{n}. \qquad (9)$$

The subscript i denotes the points of the interface belonging to bubble 1 (acceptor), and subscript j denotes the points of the interface belonging to bubble 2 (donor). Hence, $\mathbf{f}_{ij}$ is the repulsive force acting on point i contributed from a few approaching points j on the interface of bubble 2. The distance
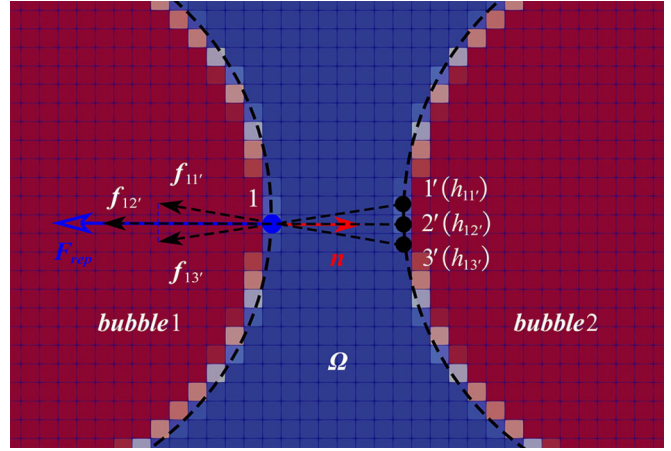

FIG. 1. Schematic representation of the near interaction forces between two approaching bubbles. Here, $\mathbf{n}$ (with a red arrow) is the unit normal vector of the surface for bubble 1 at point 1 (acceptor cell), and $h_{ij}(h_{11'}, h_{12'}, h_{13'})$ is the distance from the points $1'$, $2'$, $3'$ (donor cells) of bubble 2 to their acceptor (point 1 at bubble 1). The resultant force $\mathbf{F}_{\text{rep}}$(blue arrow) acting on point 1 is the sum of $\mathbf{f}_{ij}(\mathbf{f}_{11'}, \mathbf{f}_{12'}, \mathbf{f}_{13'})$ projected to the negative direction of $\mathbf{n}$, where $\mathbf{f}_{ij}$ is the repulsive force acting on point 1 by each donor. Note that all marker points at the interfaces are selected at the cell centres for simplicity.

of each approaching donor point j to the acceptor point i are denoted as h_{ij}. By projecting the repulsive force $\mathbf{f}_{ij}$ from point j to point i along the negative direction of the unit normal vector $\mathbf{n}$ and making a summation from $j = 1'$ to N, we obtain the resultant force $\mathbf{F}_{\text{rep},i}$ acting on point i. From Eq. (9), we see that the direction of $\mathbf{F}_{\text{rep}}$ is opposite to $\mathbf{n}$.

A similar approximation has been introduced previously to study the spreading of liquids on solids [28]. In their study, a disjoining pressure arising from molecular forces was introduced and customarily divided into several contributions. The first molecular contribution to disjoining pressure arises from London/van der Waals dispersion, which depends approximately on $1/h^3$ or $1/h^4$, where h is the gap thickness. In our model, we must emphasize that it is applied to a coarser mesh, to approximate the repulsive forces which would be observed in a finer mesh, if the computational resource allows.

In this model, we assume that the repulsive force is inversely proportional to the third power of distance, as shown in Eq. (9), which is a reasonable approximation to the short-range phase interaction. Here, K is the controlling parameter which represents the providing energy of near-contact forces to resist the approach of phase interfaces, clearly implied from its dimension. Therefore, the physical meaning of $\mathbf{F}_{\text{rep}}$ is the energy provided by the near-contact forces per unit volume. In our numerical implementation, we set the threshold distance for the inception of short-range contact to be $0.2D_b$, where D_b is the bubble diameter. In our code, K is a finite constant value for $h_{ij} < 0.2D_b$ and zero for $h_{ij} \geqslant 0.2D_b$.

Attention should be paid when calculating the repulsive force imposed on a bubble from its adjacent bubbles. Since the phase interface cells are identified by a global volume fraction α, a special numerical treatment is implanted to distinguish those belonging to different bubbles. Otherwise, the

TABLE I. The material properties and dimensionless parameters of bubbles. The dimensionless parameters are defined as $\text{Eo} = \rho_f g D_b^2 / \sigma$, $\text{Re} = \rho_f U_y D_b / \mu_f$, $\text{Mo} = g \mu_f^4 / (\rho_f \sigma^3)$, where U_y is the rising velocity along the direction of gravity.

Runs	Liquid	D_b (mm)	ρ_f (kg m^{-3})	μ_f (kg m s^{-1})	σ (N m^{-1})	Re	Eo	log(Mo)	S (mm)
Case A	80 wt. % glyc.	3.15	1208.5	60.1×10^{-3}	6.5×10^{-2}	7.39	1.81	-3.4	4
Case B	60 wt. % glyc.	3.18	1153.8	10.8×10^{-3}	6.77×10^{-2}	78.1	1.69	-6.4	4
Case C	40 wt. % glyc.	3.23	1099.3	3.72×10^{-3}	6.95×10^{-2}	256.3	1.62	-8.3	4
Case D	20 wt. % glyc.	3.22	1046.9	1.76×10^{-3}	7.09×10^{-2}	545.9	1.50	-9.6	4

contributions from the same bubble tend to tear apart the interface. We calculate the unit normal vectors $\mathbf{n_1}$, $\mathbf{n_2}$ of two adjacent interface cells, as their distance is $<0.2 D_b$. Their inner product is then given by

$$\psi = \mathbf{n_1} \cdot \mathbf{n_2}. \qquad (10)$$

Clearly, a simple criterion of $\psi < 0$ can determine that this pair of cells belong to two different bubbles.

We note that, by introducing the localized near-contact forces, the interactions between many bubbles can be simulated easily and efficiently with no need to solve extra transportation equations [18]. Moreover, the form of the repulsive force term added into the moment equation, Eq. (2), is a body force which only appears in the interface cells. It can be heuristically interpreted as a simplified model of the short-range molecular forces acting at the nanometer and subnanometer scales. The key control parameter K can be measured according to the previous experimental results [4]. Since the repulsive forces play roles only in the interface cells, $<1\%$ of all computational cells, and more importantly, the interfaces are simply identified by the volume fraction, the extra computational cost for the repulsive force model can be ignored.

III. MODEL VALIDATIONS

In this section, two previous experiments are referred for model validations [2,4]. Both of them considered a pair of deformable gas bubbles rising side by side in a quiescent liquid. Following closely the experimental setup, we release two identical bubbles from the bottom of a numerical tank. The bubbles are initially spherical and located in the same horizontal plane, with their mass centers separated by a distance S. The initial height of the bubbles from the bottom of the tank is D_b. The schematic of the computational domain is illustrated in Fig. 2. The computational domain is a cuboid, with the dimensions of $12 D_b \times 20 D_b \times 12 D_b$, sufficiently large to minimize the boundary effects. The computational domain is discretized by uniformly distributed cubic cells or Cartesian grids. The two bubbles start to rise simultaneously driven by the buoyancy force, differentiating from the experiments [2,4] in which they were injected from submerged nozzles. A total pressure boundary condition is imposed at the top outlet boundary, and no-slip boundary conditions are imposed at the side and bottom walls.

A. Bubbles rising in a water-glycerol mixture

The first experiment was performed in a water-glycerol mixture [4]. By adjusting the proportion of water and

glycerol, the liquid viscosity and therefore the bubble Reynolds number were varied, resulting in different rising behaviors of the bubbles. For example, a single rising bubble varies from spherical to ellipsoidal and then wobbling shape as the Reynolds number increases. Here, we consider four different mixture ratios, with their parameters listed in Table I. For the numerical simulations of bubbles, the required mesh resolution is important to capture their deformations as well as the detailed flow structure near the interface. The resolution tests of a single rising bubble have been investigated based on the FT [29] and LS [30] methods. The authors suggested that 30 points along the bubble diameter would be sufficient. In this paper, mesh independence tests of a single rising bubble have also been performed. We choose the mixture of case B as shown in Table I. The initial location of the bubble is at the center of the vertical cross-section of the computational domain. After reaching a steady state, the bubble remains at the center of the vertical cross-section, exhibiting a steady motion following a straight line, as shown in Fig. 3, in good
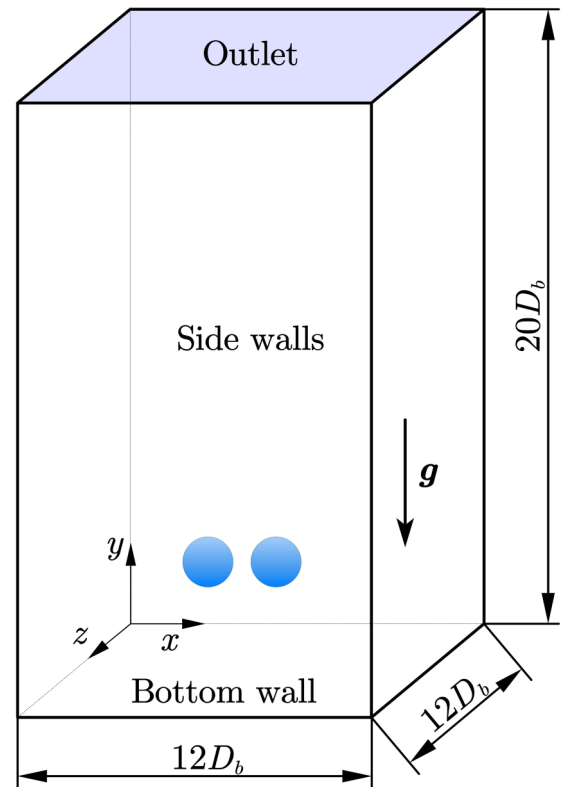

FIG. 2. Sketch of the computational domain for the simulations of a pair of bubbles rising in a viscous liquid.
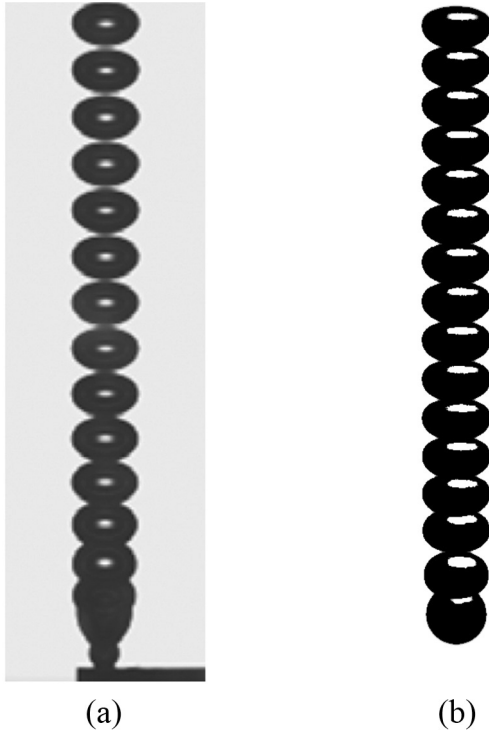
(a)   (b)

FIG. 3. The spatial and temporal evolutions of the shape of a single bubble rising in the 60 wt. % glycerol (case B in Table I), obtained by (a) the previous experiments [4] and (b) the current numerical simulations. The trajectories are displayed by overlaying the images at different time instants. The time interval between the two sequential experimental images is 10 ms, and that for the numerical simulation is 9 ms.
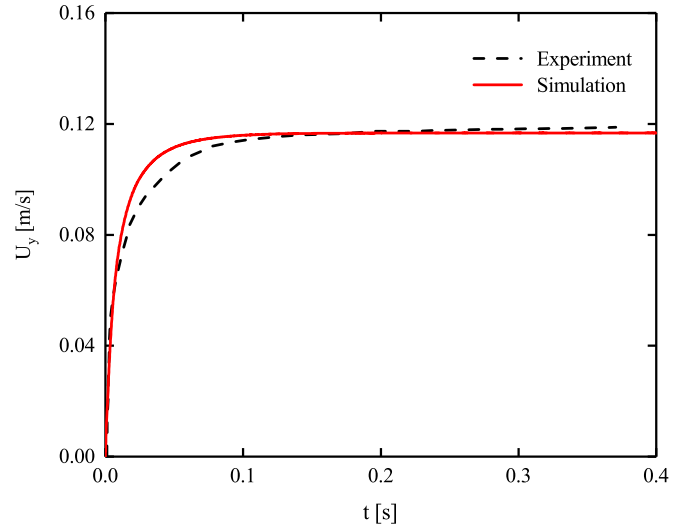

FIG. 4. Time histories of rising velocities along the direction of gravity for a single bubble in the 80 wt. % glycerol (case A in Table I). Here, the experimental data is extracted from the previous experiments [4], and the numerical result is obtained with $\Delta = D_b/30$.

agreement with the experimental observation [4]. We note that the bubble becomes ellipsoidal as it rises. Three different mesh resolutions $\Delta = D_b/20$, $\Delta = D_b/30$, and $\Delta = D_b/80$, corresponding respectively to 20, 30, and 80 cells along the bubble diameter, have obtained terminal rising velocities of 0.224, 0.2274, and 0.2297 m/s, respectively. The relative error between $\Delta = D_b/30$ and $\Delta = D_b/80$ is <1%. We also present a comparison with the experiments for case A with the mesh of $\Delta = D_b/30$, with good agreement reached, as shown in Fig. 4. Moreover, the grid independence tests have also been carried out for case D, with a higher Reynolds number of Re = 545.9. In that case, the bubble exhibits a wobbling rising trajectory. As shown in Fig. 5, the difference between $\Delta = D_b/30$ and $\Delta = D_b/60$ is very small, with the relative error in the mean rising velocity ∼0.8%. Therefore, compromising between the computational consumption and the accuracy, we choose the resolution with 30 cells along the bubble diameter, which can provide satisfactory accuracy for a 3D simulation.

The general dynamic process of two bubbles rising side by side can be described as follows. After the bubbles are released, the bubbles start to rise and change their shapes. For a certain initial separation distance, owing to the wake interactions at the early period, the bubbles are attracted to each other. When they approach a certain distance, the pressure in the film between the bubbles increases, resulting in a deformation of the bubbles. This increasing pressure induces a repelling force and drains the liquid out of the film. Then

the bubbles continue to approach each other on account of inertia and surface tension, increasing the radius of the film while decreasing the film thickness. In physical experiments, the repelling force is only derived from the pressure feedback of the thin film. However, in numerical simulations, it comes from two parts: the pressure feedback and the added repulsive force model which is designed to compensate the defect of mesh resolution. The inertia and surface tension promote the coalescence, while the repelling force prevents the coalescence. Therefore, the interacting process of bubbles can be represented as the competition between inertia, surface forces, and repelling force. When the repelling force plays
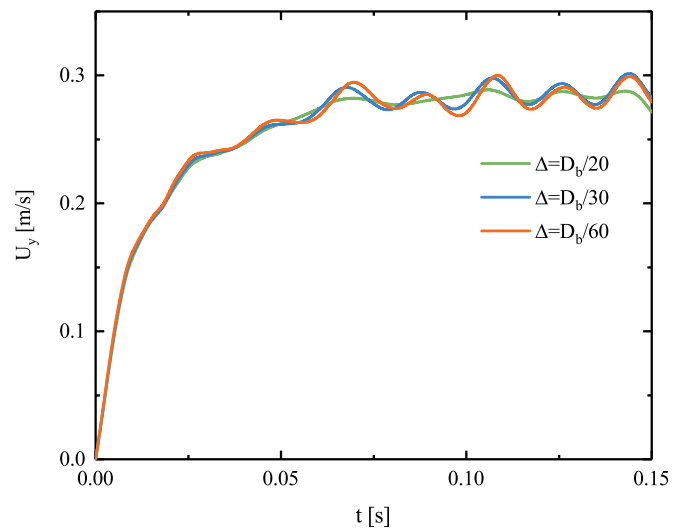

FIG. 5. Time histories of rising velocities along the direction of gravity for a single bubble in the 20 wt. % glycerol (case D in Table I). Here, $\Delta = D_b/20$, $\Delta = D_b/30$, and $\Delta = D_b/60$ correspond respectively to 20, 30, and 60 cells along the bubble diameter.
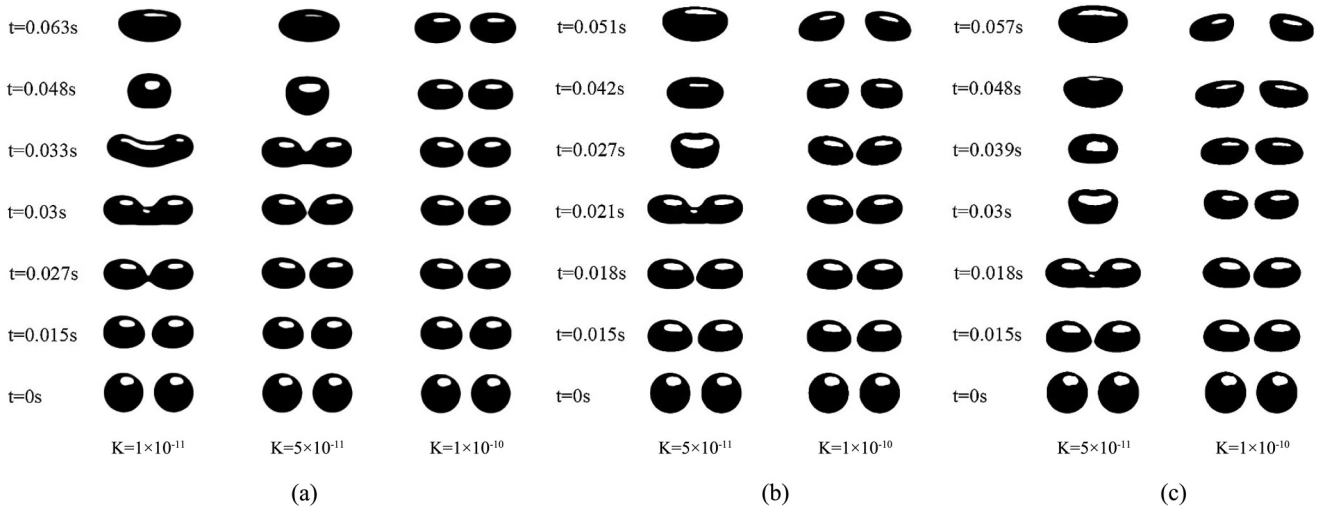
FIG. 6. The influence of control parameter K on the rising bubble pair for different water-glycerol mixtures. With the increase of K from 1×10^{-11} to 1×10^{-10} J, the bubble pair changes its behavior from numerical coalescence to bounce. Here, (a) corresponds to the bubbles in 60% glycerol solutions (case B in Table I), (b) corresponds to the bubbles in 40% glycerol solutions (case C in Table I), and (c) corresponds to the bubbles in 20% glycerol solutions (case D in Table I).

a dominant role in this process, the approaching motion of bubbles is arrested before coalescence; thereby, they bounce off.

As mentioned in Sec. II C, the coefficient K is a free parameter which can be used to tune the repulsive forces, thus playing a significant role in the process of coalescence or bounce. It is straightforward to note that, by varying the magnitude of the repulsive force, it is possible to promote or inhibit the coalescence of the colliding bubbles. Clearly, an appropriate value of K should be calibrated by the experiments to replicate the physical process. As far as this paper is concerned, the physical coalescence of a pair of bubbles is not only controlled by the material properties but also influenced by the initial separation distance S, as addressed in the previous experiments [2].

To determine the critical value for K, we carry out the tests at different cases according to Table I, as shown in Fig. 6. It is worth noting that, for case A (see Table I), in which the terminal bubble shape is spherical, the repulsive force is unnecessary to prevent coalescence. In other words, at this specific initial separation distance of 4 mm, case A presents no numerical coalescence with the current mesh resolution, even if the value of K is set to 0. Therefore, case A is not included in the tests presented in Fig. 6. Examining case B, as shown in Fig. 6(a), we see that the bubbles vary from spheres to ellipsoids, shortly after being released. For the smaller value of $K = 1 \times 10^{-11}$ J, the earlier numerical coalescence occurs at $t = 0.027$ s compared with the larger value of $K = 5 \times 10^{-11}$ J, in which case the coalescence occurs at $t = 0.03$ s. It indicates that the larger K delays the numerical coalescence. By further increasing the magnitude of K to a critical value of $K = 1 \times 10^{-10}$ J, the two bubbles bounce off without coalescing, resembling that observed in the experiment [4]. In the other two tests [Figs. 6(b) and 6(c)], this critical value of $K = 1 \times 10^{-10}$ J is also proved to be able to prevent the numerical coalescence and reproduce the bouncing collision successfully, in accord with the experimental observations [4].

The evolving process of bubble pair rising in the 80% glycerol solutions (case A in Table I), comparing with the experimental images [4], is shown in Fig. 7(a). In this case, the bubbles remain approximately spherical during the whole process, and the distance between them increases with the rising height. The horizontal velocities of the bubbles become stronger once the repulsion starts until they reach the maximum values. After that, the horizontal velocities gradually become weaker as the bubbles rise. The predicted rising behavior is also in good agreement with a previous numerical simulation [31] in which two spherical bubbles will repel each other at the low Reynolds regime. We note that, in this process, since the gap width between bubbles is always $>0.2D_b$, which is the critical distance for short-range repulsion, the artificial repulsive force is not considered. To reveal its underlying physical mechanisms, we present the instantaneous slice contours for z vorticity for case A as well as that of a single bubble for comparison in Fig. 8. We observe that the diffusion of the vorticity field around the surface of bubbles covers a relatively larger region than the separation distance. As discussed in the previous study [32], the presence of a neighboring bubble produces an asymmetric flow field, and the vorticity distributions are compressed within the gap, resulting in lateral repulsive forces.

The evolution of a bubble pair rising in the 60% glycerol solutions (case B in Table I) is shown in Fig. 7(b). Their rising velocities, horizontal velocities, and separation distance varying with the height are shown in Fig. 9. Differentiating from the low Reynolds number regime (spherical bubbles in case A), here, for Re $\sim O(10)$, the bubbles become ellipsoidal as they rise. It is shown that the bubbles first attract each other and bounce off after kissing. In the end, the bubbles rise in their respective rectilinear paths with a nearly unchanged separation distance. In contrast to the experimental observation [4], our numerical simulation presents a smaller final equilibrium distance, which might originate from the different way that the bubbles are released. In the experiments, first, the
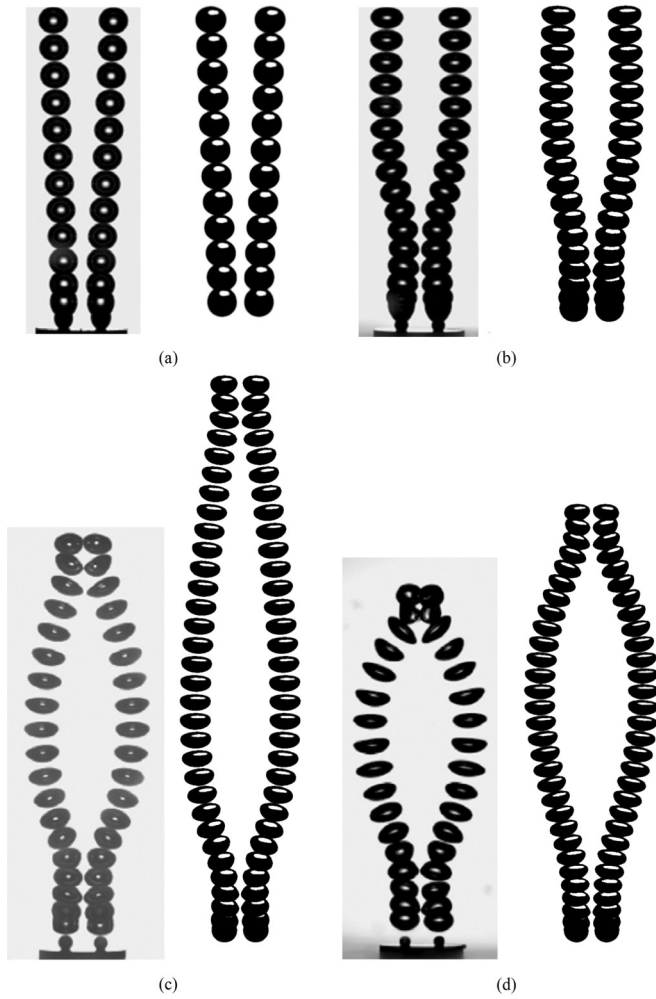
FIG. 7. Trajectories of bubble pair rising in different water-glycerol mixtures with the control parameter $K = 1 \times 10^{-10}$ J, shown by overlaying the images at different time instants. Here, (a)–(d) correspond respectively to cases A–D listed in Table I. The experimental results [4] are shown at the left side of each panel, and the current numerical simulations are shown at the right side. In (a), the time interval between two sequential experimental images is 25 ms, and that for the numerical simulation is 27 ms. For (b)–(d), the time intervals are 10 and 9 ms, respectively, for the experiments and simulations.

bubbles were released from two orifices, making it difficult for the two bubbles to detach perfectly from the orifices at the same time. A slight difference of detachment between the two bubbles and a small perturbation during this stage would lead to a largely different interaction. Second, the bubbles were released continuously, though with a small flow rate of air, which was supposed to minimize the effect of preceding bubbles.

At the initial stage, we understand that the interaction is mainly due to the Venturi effect [31]: the pair of bubbles will always attract with each other after being released because of the lower pressure within the gap between the pair of bubbles. Shown in Fig. 10 is the evolution of streamwise vortices ω_y in the vicinity of the bubbles during the attraction-repulsion period. We observe that the vortex pairs are created in the gap
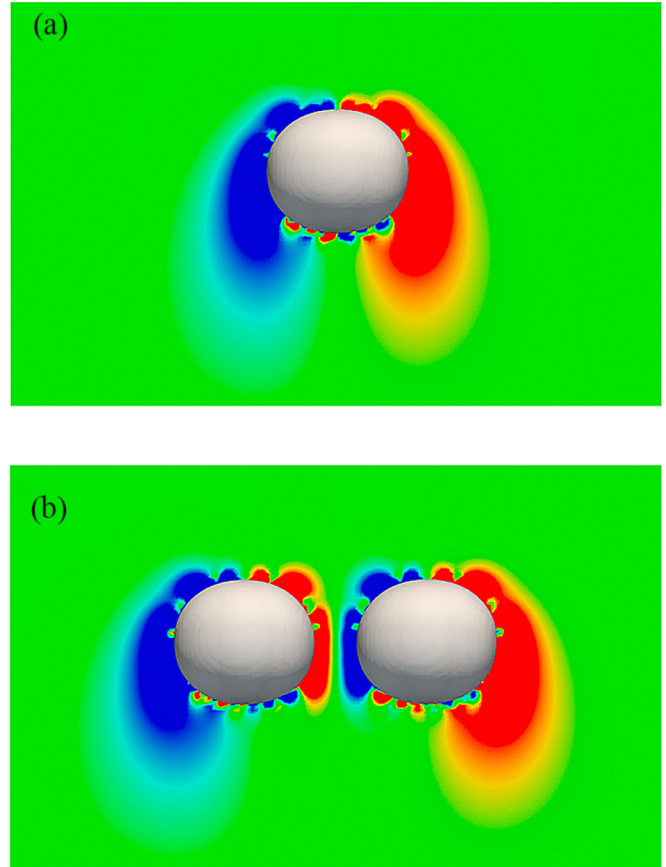

FIG. 8. The slice contours for z vorticity ($-30 s^{-1} < \omega_z < 30 s^{-1}$) around (a) a single bubble and (b) two bubbles rising in the 80% glycerol solutions (case A in Table I). The contours reveal that the vorticity diffusion is blocked on account of the presence of neighboring bubble.

when the two bubbles get close due to the higher shearing in the gap flow. During the collision, the wake-induced lift forces repel the bubbles away, while the double-threaded vortices are detached from the bubble interface. As the two bubbles are separated by some distance, no additional vorticities are
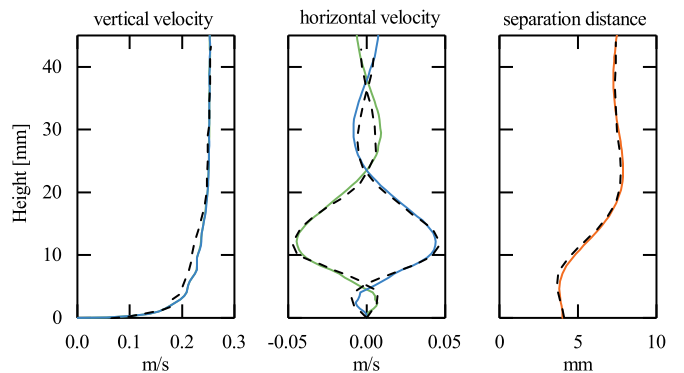

FIG. 9. Rising (vertical) velocities, horizontal velocities, and separation distance against the rising height for case B. The dashed lines represent the previous experimental results [4] and the solid lines the current numerical simulations. In the middle panel, the results for both the left and right bubbles are shown.
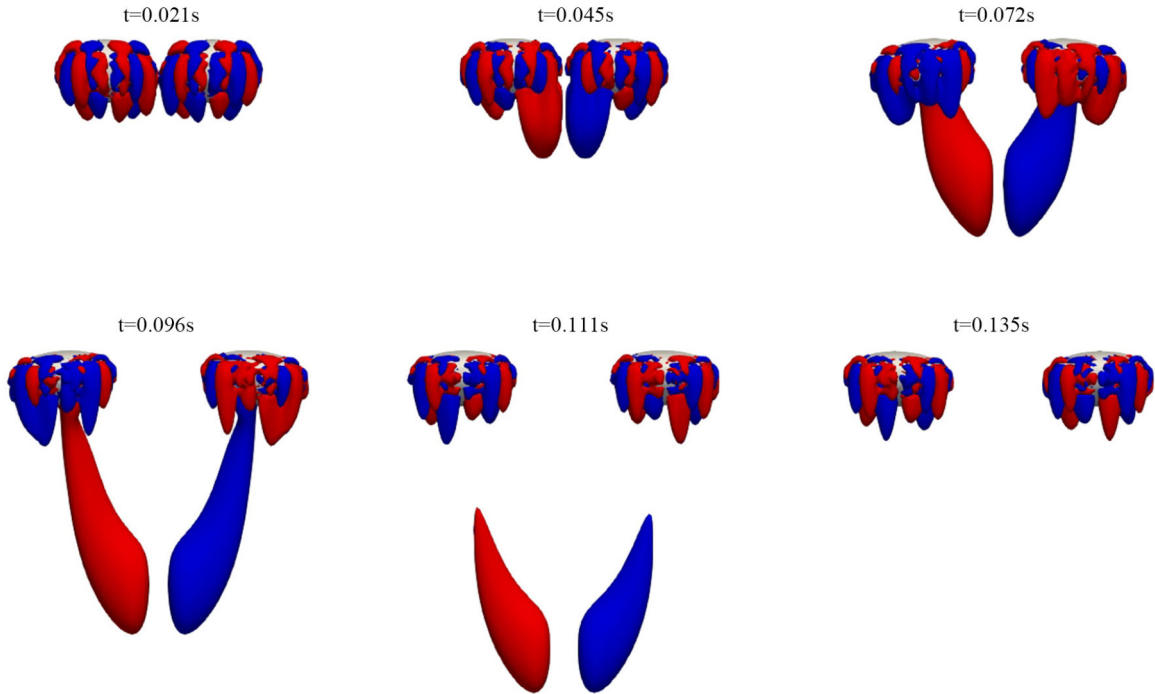
FIG. 10. Evolution of the wake structures in pairs during the collision of bubbles in the 60% glycerol solutions (case B in Table I), with the isosurfaces for z vorticity ($\omega_y = \pm 30 s^{-1}$) colored by blue for negative and red for positive values.

produced in the gap so that the double-threaded vortices disappear. We understand that the generation of double-threaded streamwise vortices are responsible for the path instability. Without the double-threaded streamwise vortices, the bubbles ultimately follow a stable rectilinear trajectory, as shown in Fig. 7(b).

As the bubble Reynolds number is further increased to Re ∼ O(100), e.g., for cases C and D in Table I, the bubbles present larger deformation, as shown in Figs. 7(c) and 7(d). Again, the bubbles attract each other and then bounce off after kissing, of which the mechanism of interaction is like case B. However, the bubbles cannot follow a stable rectilinear trajectory after collision. Instead, they keep drifting away from each other, in the currently simulated time. We present their vortical structures in Figs. 11 and 12. It is observed that the vorticities accumulate in the gap when the two bubbles get close. The wake-induced lift forces of the vortex pairs repel the bubbles away, while the double-threaded vortices are shed from the interface. Clearly, the interactions of wake structures for these strongly deformed bubbles (cases C and D) are more pronounced than the ellipsoidal bubbles (case B), separating the two bubbles further away. We note that the bubbles might retouch as they rise further due to their unstable and wobbling rising paths, as observed in the previous experiments [4], which is, however, not our major concern. The objective of this paper is to present the capability of our repulsive model on preventing numerical coalescence, which has been demonstrated in the early evolving stage.

B. Bubble pairs rising in pure water

In this section, we follow another experiment [2], in which two gas bubbles rose side by side in pure water.

In the experiments, a critical Weber number (based on the approaching velocity) was identified, below which the two equally sized bubbles were found to coalesce. Exceeding that critical Weber number, after bouncing, bubbles can either coalesce or separate without coalescing. Here, we simulate three typical combinations of bubble size and initial separation distance, corresponding to three different types of interactions, i.e., coalescence, bouncing coalescence, and bouncing separation.

In Fig. 13(a), the coalescence of bubble pairs, with D_b = 1.8 mm and the initial separation distance $S = 1.35 D_b$ is shown. The bubbles approach each other until the film between the bubbles is thinned to the critical thickness when the bubbles coalesce. From the frame of Fig. 13(a), the coalescing process is very rapid, faster than 0.002 s, from $t = 0.0195$ to 0.0215 s, where the two separate bubbles become a single dumbbell bubble. This process is consistent with the previous experimental observation [2]. The experiments explained this process from a microscopic level. They addressed that the pressure in the film between bubbles increases as the bubbles become close, resulting in a deformation of the bubbles. This increasing pressure in the film causes film drainage and a repelling force (about of the order of velocity square by Bernoulli's law) on the bubbles. The bubbles continue to approach because of inertia, which increases the radius of the film and decreases the film thickness and the bubble velocity. This thinning continues until a film thickness of the order of 100 Å is reached, the distance at which an attracting force, the van der Waals force, becomes important, resulting in coalescence. Apparently, at this subgrid scale, those forces cannot be directly resolved. Instead, they are modeled by a simple artificial repulsive force, as implemented in our numerical model.
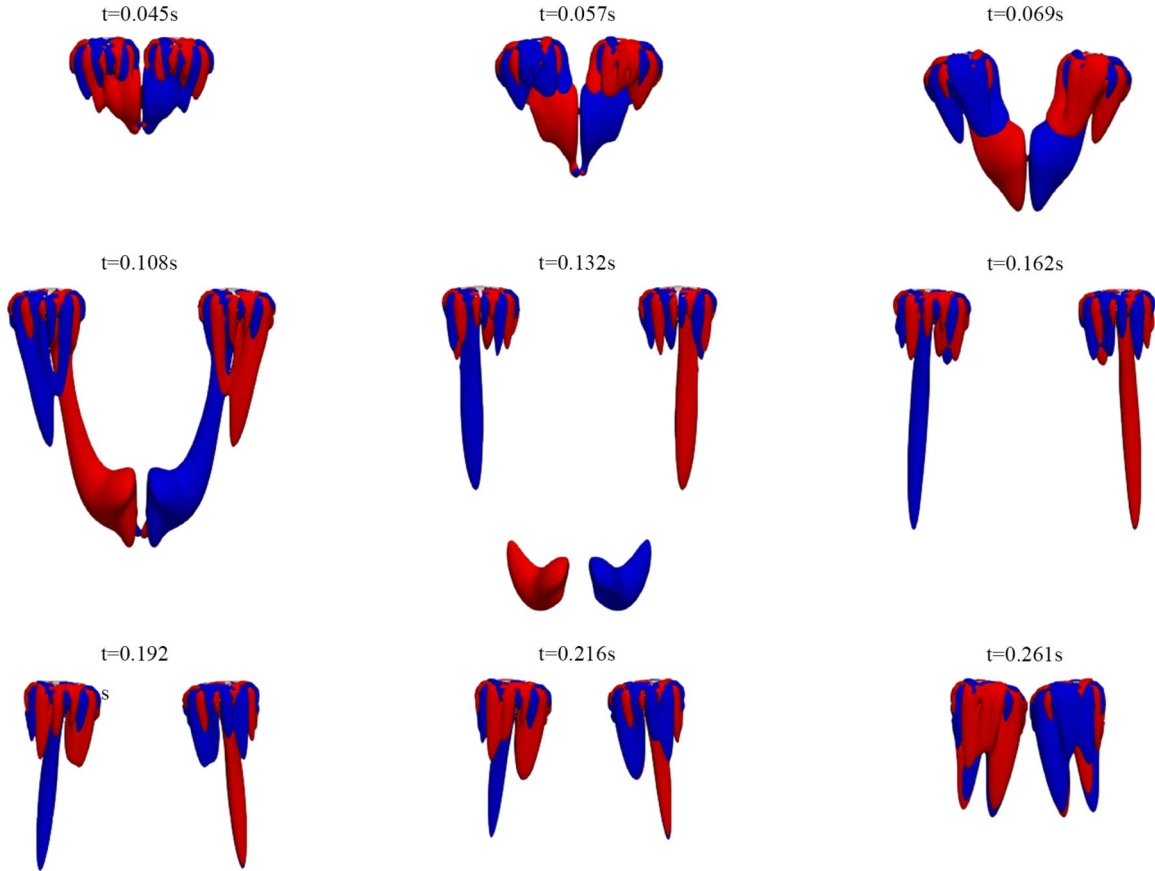
FIG. 11. Evolution of the wake structures in pairs during the collision of bubbles in the 40% glycerol solutions (case C in Table I), with the isosurfaces for z vorticity ($\omega_y = \pm 30 s^{-1}$) colored by blue for negative and red for positive values.

As the bubbles are larger or the bubble inertia is increased, the approach velocity increases, which favors the coalescence. However, on the other hand, the repelling force increases more significantly due to the increased pressure and more pronounced deformation of the bubbles, resulting in arrested approaching motion before coalescence and the bubbles bounce. As shown in Fig. 13(b), with $D_b = 2.4$ mm and the initial separation distance $S = 1.65 D_b$, the bubble pair exhibits bouncing-coalescence interactions. At the first touch ($t = 0.033$ s), the bubbles have oriented themselves. After that, the bubbles bounce off with considerable deformation. At $t = 0.041$ s, the bubbles reach the largest separation. Then the bubbles approach again while coalescing due to the decreasing inertia. It is also possible for the bubbles to retouch twice, depending on the bubble size as well as their initial separation distance, as reported in the experiments [2].

We note that the spurious oscillation of the vorticity contours in Figs. 8 and 10–12 is due to the low spatial resolution around the bubbles. Increasing the resolution or using a body-fitted mesh can solve this issue, such as that used in the previous study [32].

The aforementioned results have shown that the bubbles can approach again when the two bubbles reach the largest separation after bounce. In that case, the bubbles eventually coalesce. Here, we present another case when the bubbles eventually separate after several bounces. In Fig. 14, we show the bouncing separation of a bubble pair, with $D_b = 1.4$ mm

and the initial separation distance $S = 1.65 D_b$. Again, the bubbles orient themselves with an obtuse angle at the first touch around $t = 0.036$ s. Then they bounce off, exhibiting shape oscillations. The second bounce occurs at $t = 0.052$ s. After that, the bubbles separate considerably and move away from each other without further approaching. We note that the deformation of the second bounce ($t = 0.052$ s) is not as strong as the first one ($t = 0.036$ s). We also make a quantitative comparison in rising velocity with the experiments [2] as well as that obtained by the previous numerical simulations based on adaptive mesh refinement (AMR) technology [31]. Shown in Table II are the rising velocities obtained at the end of the first bounce provided by different means. Clearly, our repulsive model with a relatively coarse mesh resolution

TABLE II. Comparison among the experiments [2], our repulsive model, and the previous simulations based on AMR with different mesh resolutions [31].

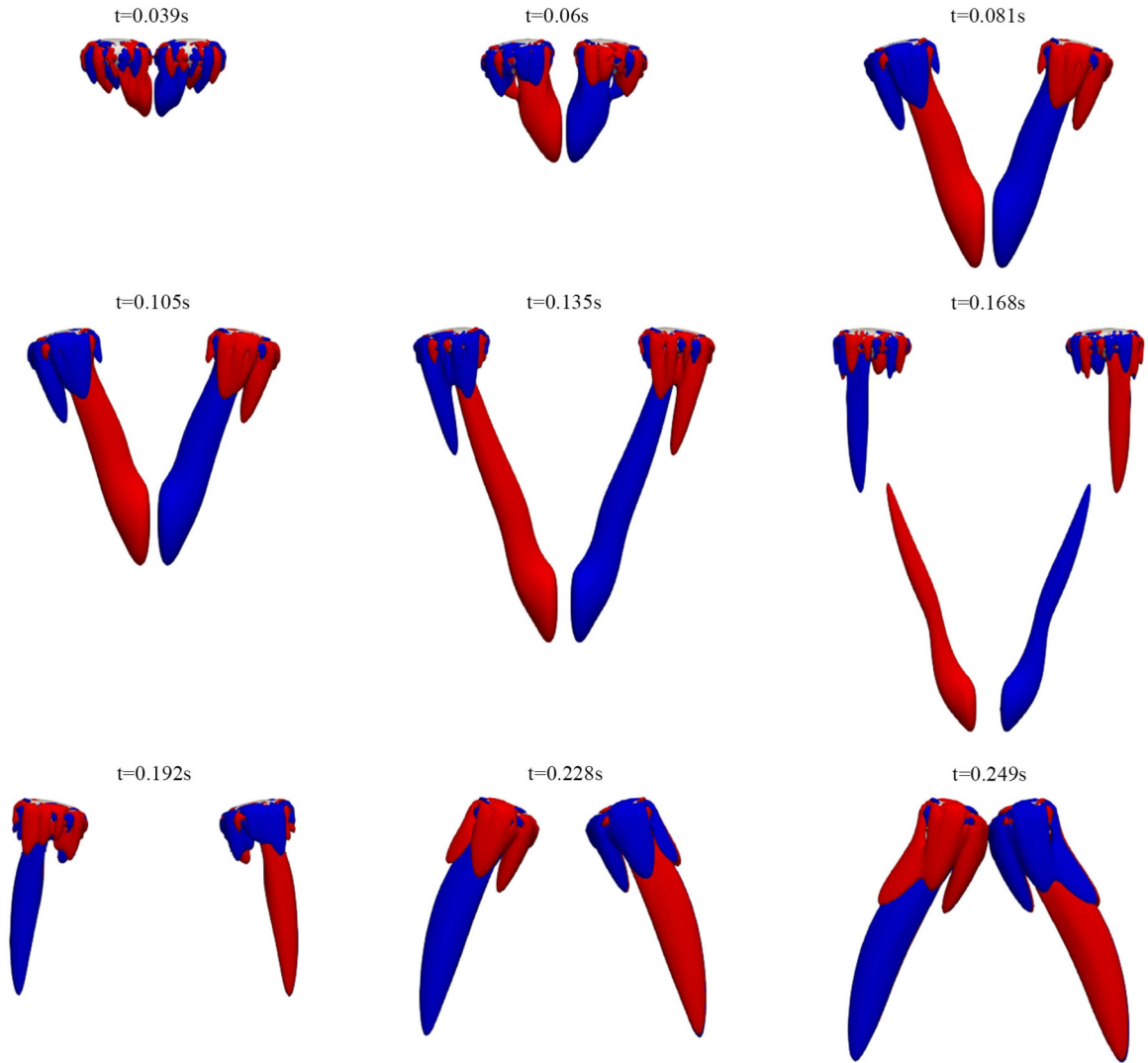| Case	Bounce	Rising velocity (m/s)
Experiment	Yes	0.26 ± 0.02
$\Delta = D_b/30$ (our model)	Yes	0.2626
$\Delta = D_b/800$ (AMR)	No	0.265
$\Delta = D_b/1600$ (AMR)	Yes	0.266
$\Delta = D_b/3200$ (AMR)	Yes	0.267

FIG. 12. Evolution of the wake structures in pairs during the collision of bubbles in the 20% glycerol solutions (case D in Table I), with the isosurfaces for z vorticity ($\omega_y = \pm 30 s^{-1}$) colored by blue for negative and red for positive values.
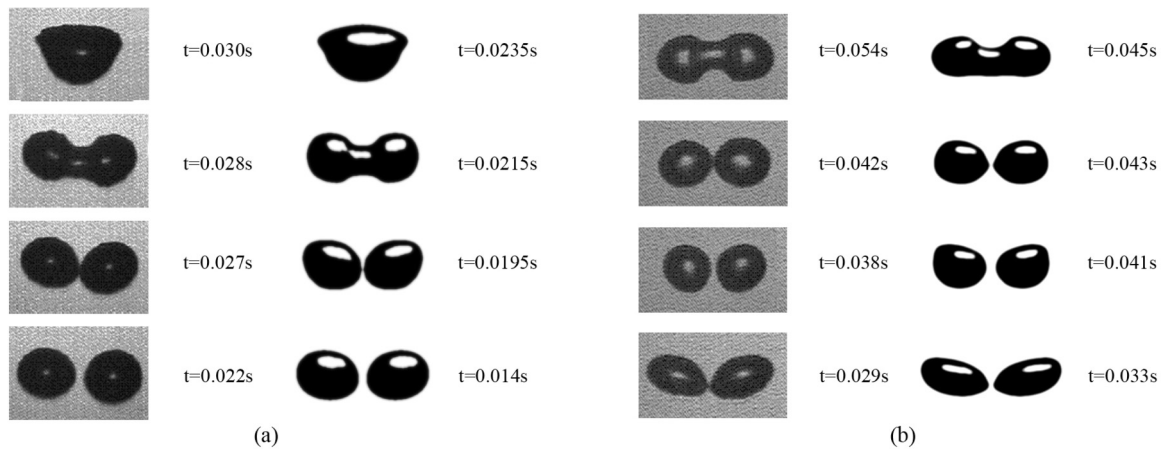

FIG. 13. (a) Bubble coalescence for $D_b = 1.8$ mm, with the initial separation distance $S = 1.35 D_b$. (b) Bouncing-coalescing bubbles for $D_b = 2.4$ mm, with the initial separation distance $S = 1.65 D_b$. The experimental results [2] are shown at the left side of each panel, and the current numerical simulations are shown at the right side.
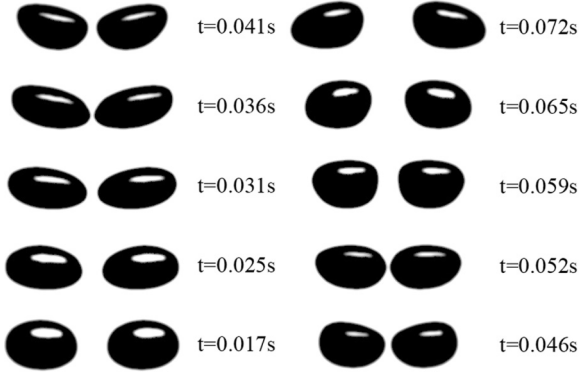
FIG. 14. Bouncing-separation bubbles for $D_b = 2.8$ mm, with the initial separation distance $S = 1.65D_b$.

provides good agreement with the experiments [2] in both predicting the bounce behavior and the accurate prediction of the rising velocity. In contrast, the numerical results based on AMR with the mesh resolution $\Delta = D_b/800$ failed to predict the bounce, where numerical coalescence occurs [31]. Furthermore, we present the time histories of rising velocity for a bubble pair with bouncing separation in Fig. 15, where the double bounces are exhibited more clearly. We observe that the rising velocity decreases slightly at the first approach and then increases due to the first bounce. When the velocity reaches a maximum value, the first bounce finishes, succeeded by the start of the second approach with a sharp drop in rising velocity. At the second bounce, the rising velocity increases again, and the whole bouncing process repeats. We note that the rising velocity after the second bounce drops deeper due to the recovery of a larger deformation. After the second bounce, the rising velocity still fluctuates but mainly owing to the instabilities of the bubble.
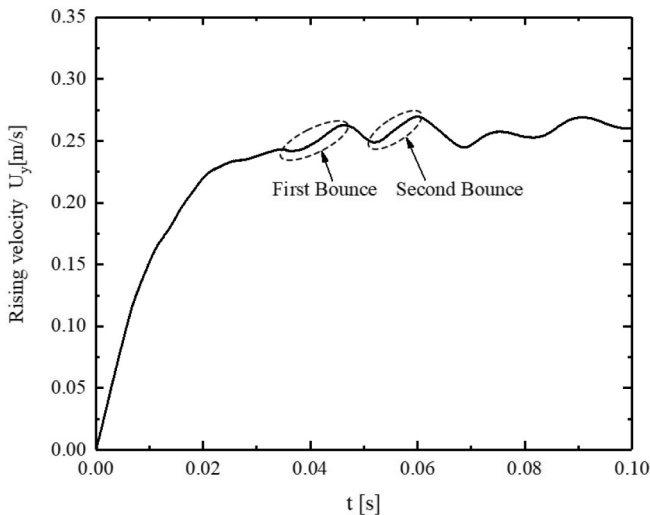

FIG. 15. Time histories of rising velocity for a bubble pair with bouncing separation. Here, the dashed lines mark the first and second bouncing processes.

IV. CONCLUSIONS

In this paper, we develop a short-range repulsive model to describe the near-contact interaction of bubbles. First of all, we calibrate the model parameter K according to the previous experiment [4]. The critical value $K = 10^{-10}$ J is determined, which can be regarded as a constant coefficient, regardless of flow regimes, for the energy provided by near-contact forces to resist the approaching process. We find that this model can be implemented for a relatively coarse mesh to prevent the nonphysical numerical coalescence of bubbles, consistent with the experimental observations [4].

Moreover, this model can also duplicate the different types of bubble-bubble interactions, as compared with another experiment [2]. In that experiment, two identical gas bubbles which rose side by side in pure water were studied. Performing the numerical simulations on three typical combinations of bubble size and initial separation distance, different types of interactions, i.e., coalescence, bouncing coalescence, and bouncing separation, are duplicated, agreeing well with the experiments [2].

Owing to the idealized simplification of underlying microscale physics by our coarse-grained repulsive model, it can investigate the behaviors with a great number of bubbles, which is very common in industrial applications. More importantly, this model can provide relatively accurate predictions with affordable computational power.

We would like to stress that a constant model parameter K has been used in this paper, which we have proved to be feasible for different types of bubble-bubble interactions. However, this coefficient is likely relevant to different parameters, such as Re and We, which will be our future concerns.

We note that this model is feasible in the range of Reynolds numbers from 5 to 500, with spherical or strongly deformable bubbles. Though it is designed for coarse mesh, a sufficient number of cells are still needed in the gap to resolve the flow within it. Here, at least 5 cells are recommended in the gap between bubbles for their initial configurations.

It should be pointed out that two bubbles with a distance of $<0.2D_b$ can experience repulsive forces even in a quiescent fluid. We have tested that, when the initial distance is $<0.2D_b$, repulsive forces arise, which separate the bubbles to a certain equilibrium distance. Therefore, we would recommend the initial separation distance to be $>0.2D_b$, which stands for all our validation cases. Actually, in real physical systems, such as bubbly flows, it is reasonable to set up a finite initial separation distance between bubbles.

APPENDIX A: REPULSION/ATTRACTION REGIMES

We demonstrate that the interacting forces between two bubbles can be either attractive or repulsive. Both can be
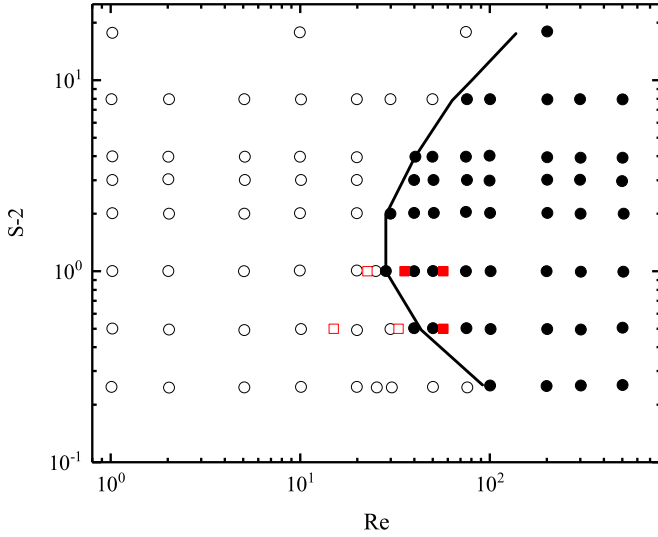
FIG. 16. Sign of the interacting forces in the (Re, S) space for two spherical bubbles rising side by side. From the previous study [32]: $\circ$, bubbles are repelled from each other, and $\bullet$, bubbles are attracted toward each other; $\square$ and $\blacksquare$ represent respectively the repulsion and attraction cases in the current numerical study. The black line divides the two regimes. S is the separation distance between bubble centers, which has been nondimensionlized by the radius.

achieved by the induced flow pressure without switching on our repulsive force model.

In the previous study [32], the flow past two identical spherical bubbles arranged side by side was studied numerically, with a zero-shear-stress condition imposed on the bubble surface to represent clean bubbles. According to the sign of transverse force, two regimes were identified in the (Re, S) parametric space, corresponding respectively to the repulsive and attractive interactions between the bubbles. Here, we select two representative separation distances $S = 2.5$ and 3.0 and vary the Reynolds number. To make a comparison, we consider a large surface tension coefficient to make sure the bubbles keep their spherical shapes during the rising process. As shown in Fig. 16, the identified transition boundary agrees well with the previous study [32]. In Fig. 16, we note that the vertical axis $S - 2$ denotes the nondimensional gap distance, which approaches zero when the two bubbles come in contact.

We should point out that, differentiating from the previous study [32], we consider two freely rising bubbles; therefore, the Reynolds numbers are calculated according to their terminal rising speed. However, since our calculated points are very close to the transition boundary, the interacting force between the bubbles is weak, leading to slightly deflected rising trajectories, as shown in Fig. 17, to ensure that our comparison with the previous work is reasonable. We also note that the shortest gap distance in the previous study was $S - 2 = 0.25$, which is larger than the threshold distance for the inception of short-range contact in our model; therefore, the repulsive force model is inactive in the simulations shown in Fig. 17. Nevertheless, it is still meaningful to validate the basic framework of our solver.
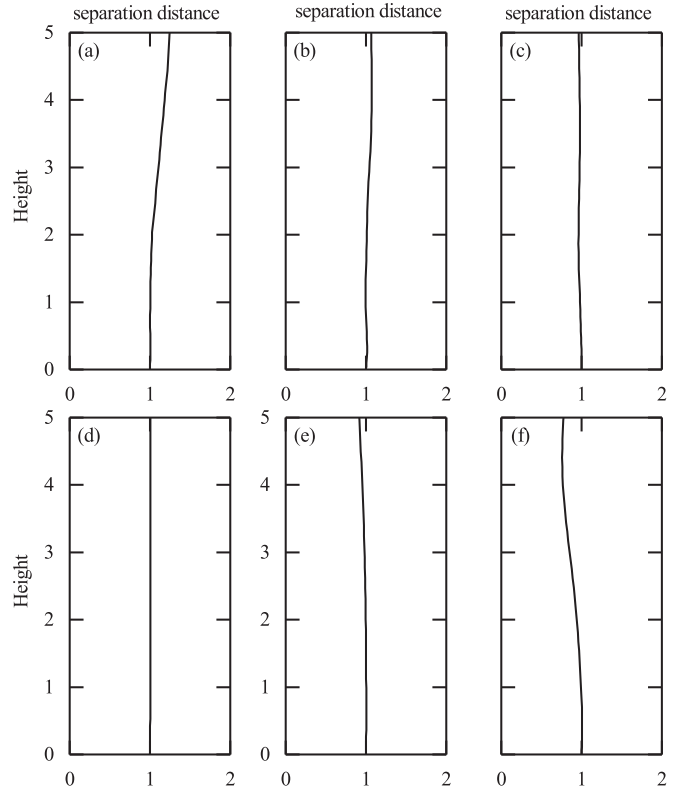

FIG. 17. The separation distance against the rising height for our near-contact model. Here, the separation distance is normalized by the initial separation distance S, and the rising height is normalized by the bubble diameter D_b. (a) $\text{Re} = 15$, $S = 2.5$; (b) $\text{Re} = 33$, $S = 2.5$; (c) $\text{Re} = 57$, $S = 2.5$; (d) $\text{Re} = 23$, $S = 3.0$; (e) $\text{Re} = 36$, $S = 3.0$; and (f) $\text{Re} = 57$, $S = 3.0$.

APPENDIX B: THE INFLUENCE OF THRESHOLD DISTANCE

For all the validation cases in the main text, a fixed threshold distance of $0.2D_b$ has been applied. However, the repulsive process of two bubbles might be different if a different threshold distance is used. Indeed, as we have tested, the threshold distance is not a unique value. Nevertheless, from Fig. 18, the threshold distances falling in the range of $0.2D_b$ to $0.4D_b$ are all acceptable. We understand that the effect of repulsive force is to push two bubbles away from each other or change their momentum. Though the peak values of repulsive forces for the three cases are different, their impulses, i.e., integration of force along time, are very close. They behave similarly in altering the momentum of the bubbles. We note that, for the case of $0.1D_b$, there are only 3 cells in the gap, which is not sufficient to resolve the gap flow.

We should also note that, as the mesh is refined, the repulsive force model may become unstable with a larger number of neighboring cells. To clarify this issue, we have presented the time histories of repulsive forces for three different resolutions in Fig. 19. The case with the finest resolution of 60 cells along the bubble diameter is still stable.
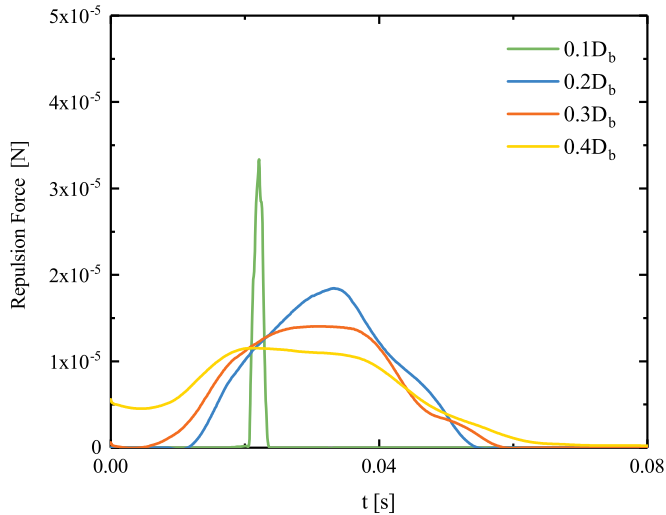
FIG. 18. Time histories of the short-range repulsive forces as two bubbles approach, considering four different threshold distances: $0.1D_b$, $0.2D_b$, $0.3D_b$, and $0.4D_b$.
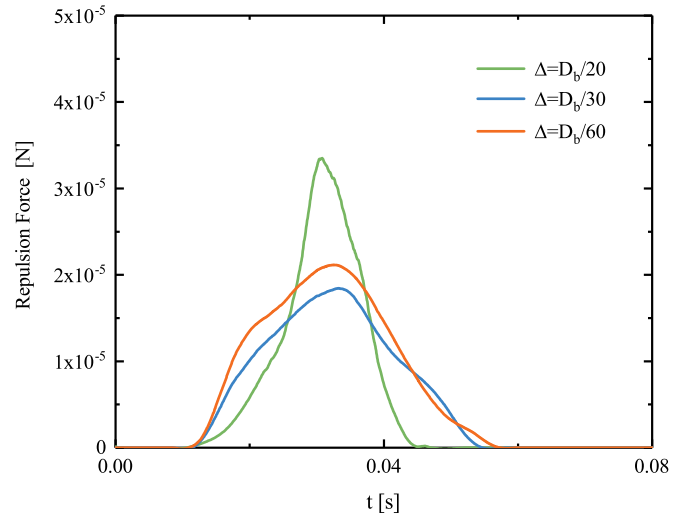

FIG. 19. Variations of the short-range repulsive force with the mesh size: $\Delta = D_b/20$, $\Delta = D_b/30$, and $\Delta = D_b/60$. It shows that the finest resolution of 60 cells along the bubble diameter is still stable.

[1] S. G. Huisman, P. Ern, and V. Roig, Interaction and coalescence of large bubbles rising in a thin gap, Phys. Rev. E **85**, 027302 (2012).

[2] P. Duineveld, Bouncing and coalescence of bubble pairs rising at high Reynolds number in pure water or aqueous surfactant solutions, in *In Fascination of Fluid Dynamics*, edited by A. Bieshevel and G. F. van Heijst (Springer, Dordrecht, 1998), pp. 409–439.

[3] A. Filella, P. Ern, and V. Roig, Interaction of two oscillating bubbles rising in a thin-gap cell: Vertical entrainment and interaction with vortices, J. Fluid Mech. **888**, A13 (2020).

[4] G. Kong, H. Mirsandi, K. Buist, E. Peters, M. Baltussen, and J. Kuipers, Hydrodynamic interaction of bubbles rising side-by-side in viscous liquids, Exp. Fluids **60**, 1 (2019).

[5] H. Kusuno, H. Yamamoto, and T. Sanada, Lift force acting on a pair of clean bubbles rising in-line, Phys. Fluids **31**, 072105 (2019).

[6] G. Tryggvason, B. Bunner, A. Esmaeeli, D. Juric, N. Al-Rawahi, W. Tauber, J. Han, S. Nas, and Y.-J. Jan, A front-tracking method for the computations of multiphase flow, J. Comput. Phys. **169**, 708 (2001).

[7] C. W. Hirt and B. D. Nichols, Volume of fluid (VOF) method for the dynamics of free boundaries, J. Comput. Phys. **39**, 201 (1981).

[8] J. Roenby, H. Bredmose, and H. Jasak, A computational method for sharp interface advection, R. Soc. Open Sci. **3**, 160405 (2016).

[9] A. Begmohammadi, R. Haghani-Hassan-Abadi, A. Fakhari, and D. Bolster, Study of phase-field lattice Boltzmann models based on the conservative Allen-Cahn equation, Phys. Rev. E **102**, 023305 (2020).

[10] S. Zhang, J. Tang, and H. Wu, Phase-field lattice Boltzmann model for two-phase flows with large density ratio, Phys. Rev. E **105**, 015304 (2022).

[11] S. Osher and R. P. Fedkiw, Level set methods: An overview and some recent results, J. Comput. Phys. **169**, 463 (2001).

[12] A. Innocenti, A. Jaccod, S. Popinet, and S. Chibbaro, Direct numerical simulation of bubble-induced turbulence, J. Fluid Mech. **918**, A23 (2021).

[13] N. M. Musehane, O. F. Oxtoby, and B. D. Reddy, Multi-scale simulation of droplet–droplet interaction and coalescence, J. Comput. Phys. **373**, 924 (2018).

[14] N. Balcázar, O. Lehmkuhl, J. Rigola, and A. Oliva, A multiple marker level-set method for simulation of deformable fluid particles, Int. J. Multiphase Flow **74**, 125 (2015).

[15] J. Zhang, M.-J. Ni, and J. Magnaudet, Three-dimensional dynamics of a pair of deformable bubbles rising initially in line. Part 1. Moderately inertial regimes, J. Fluid Mech. **920**, A16 (2021).

[16] J. Zhang, M.-J. Ni, and J. Magnaudet, Three-dimensional dynamics of a pair of deformable bubbles rising initially in line. Part 2. Highly inertial regimes, J. Fluid Mech. **943**, A10 (2022).

[17] V. Pandey, R. Ramadugu, and P. Perlekar, Liquid velocity fluctuations and energy spectra in three-dimensional buoyancy-driven bubbly flows, J. Fluid Mech. **884**, R6 (2020).

[18] L. Zhang, K. Peng, X. Shao, and J. Deng, Direct numerical simulation of deformable rising bubbles at low Reynolds numbers, Phys. Fluids **33**, 113309 (2021).

[19] C. Stubenrauch and R. Von Klitzing, Disjoining pressure in thin liquid foam and emulsion films-new concepts and perspectives, J. Phys.: Condens. Matter **15**, R1197 (2003).

[20] M. Mani, S. Mandre, and M. P. Brenner, Events before droplet splashing on a solid surface, J. Fluid Mech. **647**, 163 (2010).

[21] S. Rubin, A. Tulchinsky, A. D. Gat, and M. Bercovici, Elastic deformations driven by non-uniform lubrication flows, J. Fluid Mech. **812**, 841 (2017).

[22] V. Bergeron, Forces and structure in thin liquid soap films, J. Phys.: Condens. Matter **11**, R215 (1999).

[23] M. Kwakkel, W.-P. Breugem, and B. J. Boersma, Extension of a CLSVOF method for droplet-laden flows with a coalescence/breakup model, J. Comput. Phys. **253**, 166 (2013).

[24] J. U. Brackbill, D. B. Kothe, and C. Zemach, A continuum method for modeling surface tension, J. Comput. Phys. **100**, 335 (1992).

[25] T. Maric, H. Marschall, and D. Bothe, voFoam—a geometrical volume of fluid algorithm on arbitrary unstructured meshes with local dynamic adaptive mesh refinement using OpenFOAM, arXiv:1305.3417.

[26] L. Jofre, O. Lehmkuhl, J. Castro, and A. Oliva, A 3-D volume-of-fluid advection method based on cell-vertex velocities for unstructured meshes, Comput. Fluids **94**, 14 (2014).

[27] S. S. Deshpande, L. Anumolu, and M. F. Trujillo, Evaluating the performance of the two-phase flow solver interFoam, Comput. Sci. Discov. **5**, 014016 (2012).

[28] G. F. Teletzke, H. T. Davis, and L. Scriven, How liquids spread on solids, Chem. Eng. Commun. **55**, 41 (1987).

[29] A. Esmaeeli and G. Tryggvason, Direct numerical simulations of bubbly flows Part 2. Moderate Reynolds number arrays, J. Fluid Mech. **385**, 325 (1999).

[30] A. Loisy, A. Naso, and P. D. Spelt, Buoyancy-driven bubbly flows: ordered and free rise at small and intermediate volume fraction, J. Fluid Mech. **816**, 94 (2017).

[31] J. Zhang, L. Chen, and M.-J. Ni, Vortex interactions between a pair of bubbles rising side by side in ordinary viscous liquids, Phys. Rev. Fluids **4**, 043604 (2019).

[32] D. Legendre, J. Magnaudet, and G. Mougin, Hydrodynamic interactions between two spherical bubbles rising side by side in a viscous liquid, J. Fluid Mech. **497**, 133 (2003).